

Competition and bistability of ordered undulations and undulation chaos in inclined layer convection

KAREN E. DANIELS^{1,2}, OLIVER BRAUSCH³,
WERNER PESCH³ AND EBERHARD BODENSCHATZ^{1,4}

¹Laboratory of Atomic and Solid State Physics, Cornell University, Ithaca, NY 14853

²Department of Physics, North Carolina State University, Raleigh, NC 27695

³Physikalisches Institut der Universität Bayreuth, 95440 Bayreuth, Germany

⁴Max Planck Institute for Dynamics and Self-Organization, Göttingen, Germany

(Received 4 February 2007 and in revised form 12 October 2007)

Experimental and theoretical investigations of undulation patterns in high-pressure inclined layer gas convection at a Prandtl number near unity are reported. Particular focus is given to the competition between the spatiotemporal chaotic state of undulation chaos and stationary patterns of ordered undulations. In experiments, a competition and bistability between the two states is observed, with ordered undulations most prevalent at higher Rayleigh number. The spectral pattern entropy, spatial correlation lengths and defect statistics are used to characterize the competing states. The experiments are complemented by a theoretical analysis of the Oberbeck–Boussinesq equations. The stability region of the ordered undulations as a function of their wave vectors and the Rayleigh number is obtained with Galerkin techniques. In addition, direct numerical simulations are used to investigate the spatiotemporal dynamics. In the simulations, both ordered undulations and undulation chaos were observed dependent on initial conditions. Experiment and theory are found to agree well.

1. Introduction

Many spatially extended pattern-forming systems show non-transient steady states in which spatial and temporal correlations fall off quickly; such states are often described as exhibiting “spatiotemporal chaos” (STC). Due to the coupling of spatial and temporal degrees of freedom, STC is richer than the purely temporal chaos observed in many low-dimensional nonlinear systems. While spatiotemporally chaotic phenomena have received a great deal of attention in recent years, our understanding of STC is far from satisfactory (Cross & Hohenberg 1994; Gollub 1994; Egolf, Melnikov & Bodenschatz 1998; Egolf *et al.* 2000; Gollub & Cross 2000; Bodenschatz, Pesch & Ahlers 2000; Daniels & Bodenschatz 2002). One important issue is to reveal universal mechanisms underlying STC phenomena in quite diverse systems. In this paper, we focus on striped patterns observed, for instance, in the shifting patterns of sand dunes, in cloud street formations and in many biological systems (Cross & Hohenberg 1993). A well-investigated manifestation of STC in this setting is commonly described as defect turbulence, in which the creation, annihilation and motion of topological point defects (dislocations) continually change the local

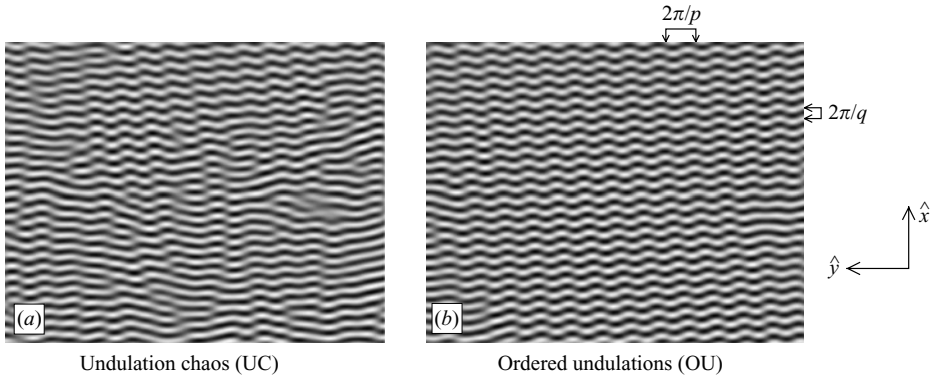


FIGURE 1. Sample shadowgraph images of a convection cell inclined by an angle $\gamma = 30^\circ$ and at Prandtl number $P = 1.1 \pm 0.04$ with reduced driving $\epsilon = 0.17$ above onset. Uphill is left; the images have been Fourier-filtered to remove higher harmonics. (a) Undulation chaos (UC) and (b) ordered undulations (OU) (Daniels & Bodenschatz 2002[†]).

wavenumber and orientation of the stripes (Coulet *et al.* 1987; Rehberg, Rasenat & Steinberg 1989; Ramazza *et al.* 1992; Bodenschatz *et al.* 2000; Daniels & Bodenschatz 2002; Young & Riecke 2003). Another feature is the bistability and competition between STC and well-ordered structures. Both may coexist in the same experimental snapshot, while in other cases the system switches between the two chaotically. While such a scenario seems to be common in many pattern-forming systems, only a few cases have been investigated in detail (Cakmur *et al.* 1997; Echebarria & Riecke 2000).

Here, we study anisotropic stripe (roll) patterns in thermal convection of an inclined fluid layer (Daniels, Plapp & Bodenschatz 2000). In particular, we present a detailed experimental study of the bistability between *ordered undulations* (OU) of stripes and the defect turbulent state of *undulation chaos* (UC)) (see figure 1). The analysis is supported by numerical simulations (Brausch 2001) of the full Oberbeck–Boussinesq equations where the OU and UC attractors were explored in a controlled manner. We characterize these two states in terms of the pattern entropy, spatial correlation length and defect density. These measures are found to be correlated with each other and are well suited to distinguish UC from OU. Along with these standard measures of STC, we determine the local wave vector of the patterns and describe the undulations of the stripes in terms of three characteristic amplitudes. These additional quantities allow a refined discrimination of OU and UC and fit well into the theoretically determined stability island of undulations.

2. Inclined layer convection

Rayleigh–Bénard convection (the thermal instability of a thin horizontal fluid layer heated from below) and its variants have been particularly fruitful in the investigation of pattern formation in extended systems (Bodenschatz *et al.* 2000). Experimentally, the use of compressed gases has allowed the construction of shallow convection cells with large lateral extent and fast time scales (de Bruyn *et al.* 1996; Bodenschatz *et al.*

[†] Movies of undulation chaos are available in AIP EPAPS Document No. EPAPS: E-PRLTAO-88-001203.

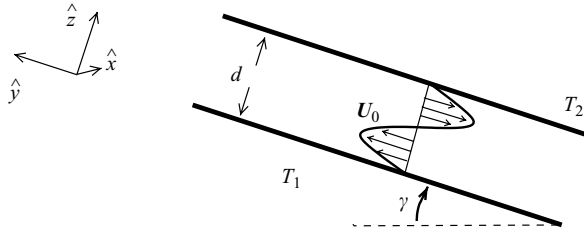


FIGURE 2. Schematic of a convection cell of thickness d inclined by an angle γ subject to a temperature difference $\Delta T = T_1 - T_2$ with associated coordinate system. U_0 indicates the induced shearflow (see text).

2000). In addition, the underlying fluid dynamical equations (Oberbeck–Boussinesq) are well established and numerical techniques have been developed to simulate systems with many convection rolls (Pesch 1996; Bodenschatz *et al.* 2000; Paul *et al.* 2004).

One natural variation of Rayleigh–Bénard convection is inclined layer convection, in which the thin fluid layer is additionally tilted by an angle γ with respect to horizontal, causing a shear flow that breaks the rotational isotropy of the layer. This situation is common in nature as convective systems are often inclined with respect to gravity. As shown schematically in figure 2, the component of gravity parallel to the layer generates a cubic shear flow profile, $U_0(z)$, upwards along the hotter (lower) plate and downward along the cooler (upper) plate. Therefore, inclined layer convection may also serve as a prototype system for convective systems in the presence of shear flow.

As in standard Rayleigh–Bénard convection, the fluid becomes unstable to convection rolls above a critical temperature difference, ΔT_c . We use the reduced control parameter $\epsilon \equiv (\Delta T / \Delta T_c) - 1$ to measure the distance from the primary instability for fixed angle of inclination γ . For a Prandtl number $P = \nu / \kappa \approx 1$ (with kinematic viscosity ν and thermal diffusivity κ) both buoyancy- and shear-driven instabilities are observed, which evolve into numerous spatiotemporally chaotic states (Daniels *et al.* 2000). In figure 3, we have reproduced the part of the phase diagram relevant for the patterns examined in this paper.

At small angles of inclination, buoyancy provides the primary instability and the convection rolls are aligned with the shear-flow direction (longitudinal rolls) (Clever 1973). Above a critical angle γ_{c2} ($\approx 78^\circ$ for the parameter regime presented here), the primary instability is shear flow driven and the rolls align perpendicularly to the shear-flow direction (transverse rolls) (Hart 1971*a, b*; Clever & Busse 1977; Ruth 1980; Ruth, Raithby & Hollands 1980).

Over a range of intermediate angles ($15^\circ \lesssim \gamma \lesssim 70^\circ$), transverse modes trigger a secondary bifurcation of longitudinal rolls to three-dimensional undulation patterns (Clever & Busse 1977) slightly above onset (see the dashed line in figure 3 at $\epsilon \approx 0.016$.) A tertiary instability to a state of crawling rolls (at $\epsilon \approx 0.3$) limits the existence region of undulations from above. For a more detailed discussion of the phase diagram, see Daniels *et al.* (2000).

Experimentally, we observed chaotic undulation patterns in the regime between the lower dashed and the upper solid destabilization line (from now on referred to as UC), where undulating convection rolls perpetually break and reconnect via moving point defects. Here, we restricted our investigations to a fixed angle of $\gamma = 30^\circ$ for a range of ϵ well inside the stability regime shown in figure 3.

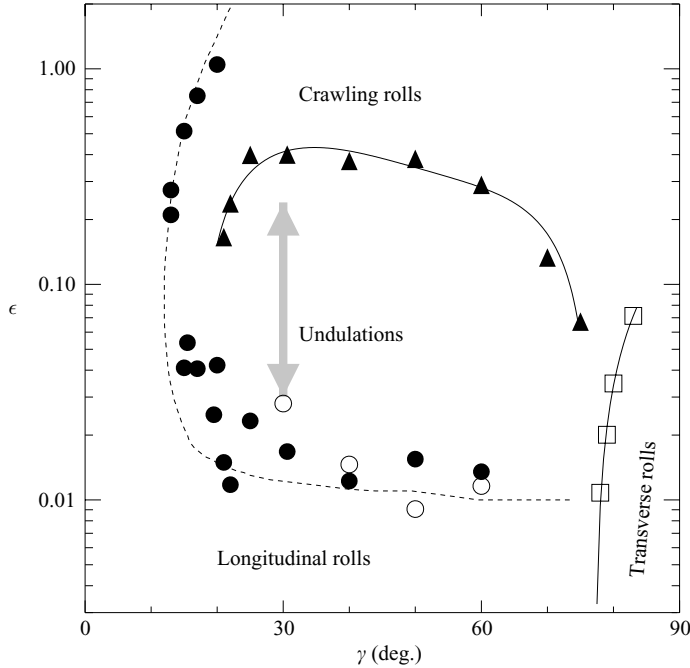


FIGURE 3. Phase diagram for inclined layer convection at $P = 1.07$ (after Daniels *et al.* 2000). Data points (and solid lines as guides to the eye) are observed boundaries between the different morphologies. The dashed line is the Galerkin prediction for the instability of longitudinal rolls to OU. The grey arrow represents the region of data collection in this paper.

inclined layer convection can serve as a paradigm for a class of anisotropic pattern-forming systems such as liquid-crystal convection (Kramer & Pesch 1995), Taylor–Couette flow (Tagg 1994), annular convection (Kurt, Busse & Pesch 2004), sand ripples (Blondeaux 1990; Hansen *et al.* 2001), or optical pattern formation (Ramazza *et al.* 1992) which also exhibit defect turbulence. In addition, it may relate to shear-flow-driven instabilities as observed in cloud street formation (Kelly 1994), Taylor–Couette flow (Andereck, Liu & Swinney 1986), Poiseuille–Bénard convection (Kelly 1977; Yu, Chang & Lin 1997; Müller, Lücke & Kamps 1992), or turbulent bursting in Couette flow (Bottin *et al.* 1998).

From here, we now proceed in §3 to explain our experimental setup and data collection. In §4, we present a theoretical analysis of inclined layer convection with an investigation of the stability of undulations and direct numerical solutions of the Oberbeck–Boussinesq equations. This analysis provides the theoretical framework we then use in §5 to perform a detailed investigation of the experimentally observed nonlinear states, including the competition between OC and UC. Finally, in §6 we present a discussion of the results and give an outlook.

3. Experiment

We conducted our experiments in a thin layer of compressed CO_2 within a rectangular cell of height $d = (388 \pm 2) \mu\text{m}$ and dimensions $(100 \times 203)d$. The CO_2 gas was 99.99% pure and the pressure was (56.5 ± 0.01) bar regulated to ± 55 mbar. The mean temperature of the convection cell was held constant at $(28 \pm 0.05)^\circ\text{C}$ regulated to ± 0.3 mK. For these conditions, the Prandtl number was $P = 1.1 \pm 0.04$

as determined from a materials property program (de Bruyn *et al.* 1996). The characteristic vertical diffusion time was $\tau_v = d^2/\kappa = (1.532 \pm 0.015)$ s. The experiments were conducted at a fixed inclination angle of $\gamma = (30.00 \pm 0.02)^\circ$. We obtained images of the convection pattern using a digital CCD camera, via the usual shadowgraph technique (de Bruyn *et al.* 1996; Trainoff & Cannell 2002).

We collected data at 17 equally spaced values of ϵ between 0.04 and 0.22, each reached by quasi-static temperature increases from below. At each ϵ , we recorded at least 400 series of 100 images (at 3 frames per second), with each series separated from others by at least $100\tau_v$ to guarantee statistical independence. These runs are later referred to as short runs. For the lowest value of $\epsilon = 0.04$, we recorded up to 600 series to cope with the reduced number of defects present in that regime. In addition, we collected data while decreasing the temperature quasi-statically from $\epsilon = 0.12$ to $\epsilon = 0.06$ to check for hysteresis, which was not observed. Particularly long time series were recorded at $\epsilon = 0.08$ (one run) and 0.17 (two runs). These consisted of six-hour ($1.4 \times 10^4 \tau_v$) runs with three pictures taken per second. These runs are later referred to as long runs.

Figure 4(a) shows a sample Fourier-filtered shadowgraph image of the complete experimental cell at $\epsilon = 0.08$. While on first sight the pattern appears to be uniformly composed of UC, detailed investigation demonstrates that this is not the case. In figure 4(b) we have superimposed 400 statistically independent images at the same ϵ (one from each short run). Clearly visible are grey regions, such as within the white-framed subregion, where the average looks almost structureless. There exist also long-term ordered regions such as the strong black/white roll patches near the boundaries. Other spatiotemporally chaotic systems (Ning, Ecke & Ahlers 1993; Gluckman *et al.* 1993) also exhibit similar behaviour due to the presence of boundaries.

Another method of characterizing the spatiotemporal homogeneity of a ‘chaotic’ pattern is to superimpose defect trajectories obtained for statistically independent frames (see §5.1 for details on defect detection). An example is shown in figure 4(c), where we superimpose defect trajectories for 50 statistically independent short runs. Defects with positive (negative) topological charge are white (black). Again, far away from the boundaries (within the marked subregion), persistent and homogeneous creation and annihilation of point defects were observed. In contrast, other regions were either rarely traversed by defects or were preferentially traversed by defects of like charge. In addition, favoured spots along the boundaries preferentially seeded defects of the same charge, which then followed similar trajectories. Thus, to minimize the impact of these effects and to utilize as ideal a cell as possible, the data presented in this paper were taken only from the subregion of dimension $51d \times 63d$ marked by the white box.

4. Theoretical description

We base our theoretical description on the standard Oberbeck–Boussinesq equations (OBE), slightly generalized to cover the inclination of the fluid layer. As in the experiments, we concentrate on systems with large aspect ratio, i.e. with the lateral dimensions of the cell in the (x, y) -plane \gg its height d in the z -direction. Thus, we adopt the usual idealization of periodic horizontal boundary conditions, which are incorporated numerically by switching from position space to two-dimensional Fourier space.

First, the onset of inclined layer convection is obtained by a standard linear stability analysis of the base state. Then, in the nonlinear regime, we investigate the

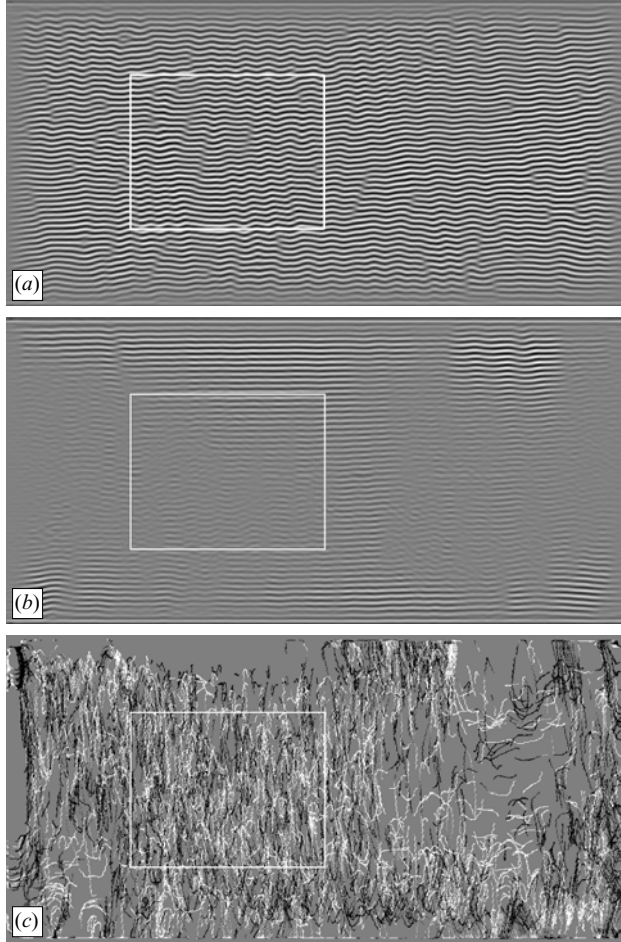


FIGURE 4. (a) Example convection cell, (b) average of 400 statistically independent images, and (c) defect trajectories for fifty statistically independent short runs. White (black) are defects with positive (negative) topological charge. The nearly homogeneous subregion ($51d \times 63d$) used in all analyses is marked by a white box. Uphill is at the left. $\epsilon = 0.08$, $P = 1.1 \pm 0.04$ and $\gamma = 30^\circ$.

stability of periodic solutions using both weakly nonlinear and multimode Galerkin approaches. Most important for the interpretation of the (weakly) disordered states in the experiments have been fully three-dimensional solutions of the OBE.

4.1. Basic equations

As shown in figure 2, the convection cell is subjected to a temperature difference $\Delta T \equiv (T_1 - T_2) > 0$ between the hot (bottom) and cold (top) plate and is inclined by an angle γ . In a coordinate system aligned with the cell, the gravity vector is given by $\mathbf{g} = -g(\hat{\mathbf{z}} \cos \gamma + \hat{\mathbf{y}} \sin \gamma)$, where g is the acceleration due to gravity. As usual we introduce the Rayleigh number R as a non-dimensional measure for ΔT :

$$R \equiv \frac{\alpha g \cos \gamma \Delta T d^3}{\nu \kappa} \quad (4.1)$$

with α the thermal expansion coefficient, ν the kinematic viscosity, κ the thermal diffusivity. Please note that R depends on γ .

The OBE become dimensionless if lengths are measured in units of d , time in units of the thermal diffusion time $\tau_v \equiv d^2/\kappa$, temperatures in units of $\Delta T/R$ and velocities in units of d/τ_v . Thus, we arrive at the following non-dimensional form of the OBE:

$$\nabla^2 \mathbf{u} + \theta \hat{\mathbf{z}} + (-Rz + \theta) \hat{\mathbf{y}} \tan \gamma - \nabla \pi = P^{-1} \left[\frac{\partial}{\partial t} \mathbf{u} + (\mathbf{u} \cdot \nabla) \mathbf{u} \right], \quad (4.2a)$$

$$\nabla^2 \theta + R \mathbf{u} \cdot \hat{\mathbf{z}} = \frac{\partial \theta}{\partial t} + (\mathbf{u} \cdot \nabla) \theta. \quad (4.2b)$$

$(\Delta T/R)\theta$ denotes the deviation from the linear temperature profile $\frac{1}{2}(T_1 + T_2) - \Delta T z$ ($-1/2 < z < 1/2$) of the basic non-convecting state. Terms which can be expressed as gradients are included in the pressure term $\nabla \pi$. We assume incompressibility of the velocity field, \mathbf{u} , i.e. $\nabla \cdot \mathbf{u} = 0$. Furthermore, θ and \mathbf{u} are required to vanish at $z = \pm 1/2$ (rigid boundary conditions).

Even below the onset of convection, the OBE provide a base flow with a cubic mean-flow profile $\mathbf{U}_0(z)$ (in dimensionless units):

$$\mathbf{U}_0(z) = \frac{R \tan \gamma}{6} \left(z^3 - \frac{z}{4} \right) \hat{\mathbf{y}}, \quad (4.3)$$

as illustrated in figure 2. Above the onset of convection, it is useful to split the solenoidal velocity field \mathbf{u} into three parts using

$$\mathbf{u} \equiv \mathbf{U}_0(z) + \mathbf{v}(x, y, z; t) + \mathbf{U}(z, t). \quad (4.4)$$

The term $\mathbf{v}(x, y, z; t)$ is derived from a poloidal-toroidal decomposition of \mathbf{u} in the form $\mathbf{v} = \mathbf{v}_{pol} + \mathbf{v}_{tor} \equiv \nabla \times \nabla \times (\hat{\mathbf{z}} \chi) + \nabla \times \hat{\mathbf{z}} \zeta$ with the poloidal (toroidal) velocity potentials χ (ζ). This decomposition automatically fulfills $\nabla \cdot \mathbf{v} = 0$. The field $\mathbf{v}_{pol}(x, y, z; t)$ describes the periodic convection rolls with their (nearly circular) streamlines and vanishing vertical vorticity $\Omega_z = (\nabla \times \mathbf{u})_z$, while \mathbf{v}_{tor} is associated with finite Ω_z .

Convection also leads to a modification $\mathbf{U}(z, t)$ (see (4.4)) of the basic shear-flow profile $\mathbf{U}_0(z)$. The governing equations for $\mathbf{U}(z, t) = (U_x(z, t), U_y(z, t), 0)$, derive from a horizontal average of (4.2a) and read as follows:

$$(\partial_{zz}^2 - P^{-1} \partial_t) U_x + P^{-1} \partial_z [\overline{v_x v_z}] = 0, \quad (4.5a)$$

$$(\partial_{zz}^2 - P^{-1} \partial_t) U_y + P^{-1} \partial_z [\overline{v_y v_z}] + \bar{\theta} \sin \gamma = 0. \quad (4.5b)$$

Here, the overline denotes an in-plane average (the $\mathbf{q} = 0$ component in Fourier space) of the corresponding terms. Note that (4.2) become γ -independent for longitudinal rolls which vary only in the x -direction. Thus the onset of longitudinal rolls and their structure (but not their stability) can be deduced immediately from the standard Rayleigh-Bénard problem without inclination (Clever 1973).

While \mathbf{v}_{tor} vanishes in perfectly-periodic roll patterns, it is usually excited by any imperfections, such as roll curvature or pattern defects. In contrast to \mathbf{v}_{pol} , the Hagen-Poiseuille-like z -profile of \mathbf{v}_{tor} is even in z , and is often referred to as mean flow. Other fields can thus be efficiently advected by \mathbf{v}_{tor} , typically leading to further enhancement of some initial perturbation. For Prandtl number of order unity and below, the resulting positive feedback is the source of spatiotemporal complexity as observed in defect turbulence (Daniels & Bodenschatz 2002) and spiral defect chaos (Morris *et al.* 1993).

4.2. Periodic solutions

It is convenient to substitute (4.4) into (4.2) and to use a condensed notation for the resulting OBE equations:

$$\mathcal{C} \frac{\partial}{\partial t} \mathbf{V}(\mathbf{x}, z, t) = \mathcal{L} \mathbf{V}(\mathbf{x}, z, t) + \mathcal{N}(\mathbf{V}, \mathbf{V}). \tag{4.6}$$

The fields $\chi, \zeta, \theta, \bar{\mathbf{u}}$ have been collected into a symbolical vector \mathbf{V} . The letters \mathcal{C} and \mathcal{L} represent the resulting linear operators and \mathcal{N} the quadratic nonlinearities in (4.2) and (4.5).

The first step in any theoretical investigation is the linear stability analysis of the base state $\mathbf{V} = 0$. Neglecting \mathcal{N} in (4.6), we arrive at a linear eigenvalue problem which diagonalizes in Fourier space via the ansatz $\mathbf{V}(\mathbf{x}, z, t) = e^{\lambda t} e^{i\mathbf{q}\cdot\mathbf{x}} \mathbf{V}_{lin}(\mathbf{q}, z)$ with $\mathbf{x} = (x, y)$ and $\mathbf{q} = (q, p)$. The eigenvalue $\lambda(\mathbf{q}, R) = \sigma + i\omega$ with the largest real part provides the growth rate $\sigma(\mathbf{q}, R)$. The condition $\sigma(\mathbf{q}, R) = 0$ describes the neutral stability curve $R_0(\mathbf{q})$ which has a minimum at $R_c = R_0(\mathbf{q}_c)$ for the critical wave vector \mathbf{q}_c . In the present case, we find $\omega = 0$, so the bifurcation is stationary.

In contrast to isotropic systems, where $\sigma(\mathbf{q})$ and $R_0(\mathbf{q})$ depend only on the modulus of \mathbf{q} , the anisotropy causes them to depend in addition on the angle between \mathbf{q} and $\hat{\mathbf{y}}$. Inspection of (4.2) shows that the control parameter R appears not only explicitly in the buoyancy term of (4.2b), but also in the coefficient $P^{-1}R \tan \gamma$ arising from the U_0 contributions (see (4.3)) to the advection terms (see (4.4)).

Where buoyancy prevails (γ less than the critical angle $\gamma_{c2}(P)$), we find longitudinal rolls at the onset of convection, with $\mathbf{q}_c = (q_c, 0)$. The threshold $R_c = 1708$ (defined according to (4.1)) and $q_c = 3.117$ are γ -independent. In contrast, for $\gamma > \gamma_{c2}$ the instability is shear flow driven and transverse rolls with $\mathbf{q}_c = (0, p_c)$ are selected. This critical behaviour at threshold was discussed in Hart (1971a, b); Clever (1973); Clever & Busse (1977); Ruth *et al.* (1980).

We use Galerkin methods to study ideal periodic convection patterns in the nonlinear regime. All fields are expanded in two-dimensional Fourier series with respect to the (x, y) -coordinate plane and in suitable test functions in z fulfilling the rigid boundary conditions at $z = \pm 1/2$. For instance, the θ component of \mathbf{V} reads

$$\theta(\mathbf{x}, z; t) = \sum_{k,m} \left[\exp [i(kqx + mpy)] \sum_n c_{k,m;n}(t) S_n(z) \right] \tag{4.7}$$

with $S_n(z) = \sin(n\pi(z + 1/2))$. To ensure real-valued θ , we require $c_{-k,-m;n} = c_{k,m;n}^*$. The fields χ, ζ are analogously represented except that we use the Chandrasekhar functions $C_n(z)$ (Chandrasekhar 1961) instead of the $S_n(z)$ for χ .

For longitudinal rolls ($\mathbf{q} \parallel \hat{\mathbf{x}}$), all coefficients with $m \neq 0$ vanish; conversely, for transverse rolls ($\mathbf{q} \perp \hat{\mathbf{x}}$) all coefficients with $k \neq 0$ vanish. By inserting (4.7) and the analogous expansions for $\chi, \zeta, \bar{\mathbf{u}}$ into (4.6) and truncating the series one arrives at a nonlinear algebraic system for the their expansion coefficients. This system of equations is solved using a Newton–Raphson iteration scheme and subsequently tested for stability with respect to linear perturbations. Using the standard Floquet ansatz, the θ perturbation reads for instance

$$\delta\theta(\mathbf{x}, z; t) = e^{\sigma_n t} e^{i\mathbf{s}\cdot\mathbf{x}} \sum_{k,m} \left[\exp [i(kqx + mpy)] \sum_n \delta c_{k,m;n} S_n(z) \right], \tag{4.8}$$

with $\mathbf{s} = (s_x, s_y)$. Positive nonlinear growth rates $\text{Re}[\sigma_n(\mathbf{q}, \mathbf{s}, R, P)]$ signal secondary instabilities of the periodic convection patterns. Our numerical results agree with all those published previously in the literature (e.g. Clever & Busse 1977).

This paper investigates the secondary modulational wavy (zig-zag undulation) instability of longitudinal rolls at $R = R_u(\gamma, P)$. This instability is initially characterized by transverse undulations along the roll axis at large wavelength ($s_x = 0$ and $s_y \rightarrow 0$) as first described in Clever & Busse (1977), Ruth *et al.* (1980); it develops for $R \geq R_u$ slightly above R_c , i.e. at a small reduced control parameter $\epsilon_u(P, \gamma) \equiv (R_u - R_c)/R_c$. For example, $\epsilon_u = 0.016$ for $\gamma = 30^\circ$ on the dashed line in figure 3.

Weakly nonlinear analysis provides some insight into the underlying physical mechanisms of the instability, particularly the final-amplitude state. We utilize a set of coupled, complex amplitude equations, which can be expected to work reliably for small ϵ .

We use the following ansatz for the solution of (4.6):

$$\mathbf{V}(\mathbf{x}, z, t) = A(t)\mathbf{V}_{lin}(\mathbf{q}_1, z)e^{iq_1x} + B(t)\mathbf{V}_{lin}(\mathbf{q}_2, z)e^{iq_2x} - C(t)\mathbf{V}_{lin}(\mathbf{q}_3, z)e^{iq_3x} + \text{c.c.} + \text{h.o.t.} \quad (4.9)$$

with $\mathbf{q}_1 = (q, 0)$, $\mathbf{q}_2 = (q, p)$ and $\mathbf{q}_3 = (q, -p)$. The first term describes longitudinal rolls of wavenumber q and complex amplitude $A(t)$, while the additional terms provide transverse modulations with wavenumbers $\pm p$ and complex amplitudes $B(t)$ and $C(t)$ with $|B| = |C|$. Note that the wave vectors \mathbf{q}_i span a resonant tetrad obeying

$$\mathbf{q}_1 = \mathbf{q}_2 + \mathbf{q}_3 - \mathbf{q}_1. \quad (4.10)$$

We insert (4.9) into (4.6) and retain terms up to cubic order in the amplitudes A, B, C . After projecting onto the left linear eigenvectors $\mathbf{V}_{lin}(\mathbf{q}_i, z)$ the system reduces to a set of three coupled amplitude equations, the general structure of which is predictable from symmetry arguments:

$$\frac{d}{dt}A = (\sigma_A - b_{11}|A|^2 - b_{12}|B|^2 - b_{12}|C|^2)A + \rho_1 A^* BC, \quad (4.11a)$$

$$\frac{d}{dt}B = (\sigma_B - b_{21}|A|^2 - b_{22}|B|^2 - b_{23}|C|^2)B + \rho_2 AAC^*, \quad (4.11b)$$

$$\frac{d}{dt}C = (\sigma_C - b_{21}|A|^2 - b_{23}|B|^2 - b_{22}|C|^2)C + \rho_2 AAB^*. \quad (4.11c)$$

The linear growth rates are defined as: $\sigma_A(R) = \sigma(\mathbf{q}_1, R)$, $\sigma_B(R) = \sigma_C(R) = \sigma(\mathbf{q}_2, R) < \sigma_A$. We calculate all the nonlinear coupling coefficients $b_{ij} > 0$ and the cross-coupling coefficients $\rho_i > 0$ which characterize the resonant triad coupling. It is convenient to characterize the complex amplitudes by their moduli and phases:

$$A = |A| \exp(i\phi_A), \quad B = |B| \exp(i\phi_B), \quad C = |C| \exp(i\phi_C). \quad (4.12)$$

Two phases can be arbitrarily chosen due to translational invariance in the \hat{x}, \hat{y} directions and the choice $\phi_A = 0, \phi_B = 0$ leading to real A, B is convenient. The growth rate of the undulations is obtained by a linear stability analysis of the longitudinal-roll solutions ($|A|^2 = \sigma_a/b_{11}$ for $\sigma_a > 0$). From (4.11) we arrive at a linear eigenvalue problem for the B and C with the maximal growth rate $\sigma_u(R) \equiv \sigma_B(R) + (\sigma_A(R) + \cos(\phi_C)\rho_2 + b_{21})/b_{11}$. In good agreement with the Galerkin analysis, wavy solutions with $|A| > 0$ and $|B| = |C| > 0$ bifurcate at $R = R_u$, where $\sigma_u(R)$ crosses zero. $\sigma_u(R)$ is maximal for $\phi_C = 0$ since $\rho_2 > 0$.

In more physical terms, the undulation solution creates horizontal variations of the mid-plane temperature field, which correspond to the experimentally obtained

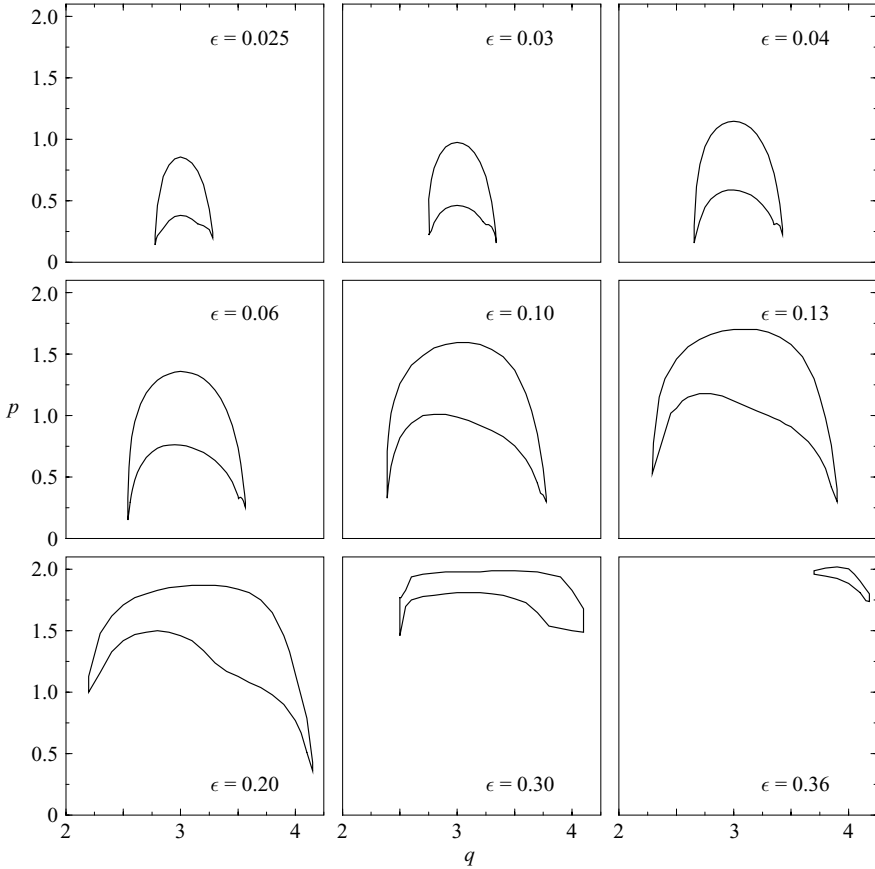


FIGURE 5. Stability islands for ordered undulations at $P = 1.14$ and $\gamma = 30^\circ$ in the (q, p) -plane at increasing values of ϵ .

shadowgraph pictures. It is convenient to normalize the temperature component of $V_{lin}(\mathbf{q}, z)$ to unity at the midplane ($z = 0$). Thus, we arrive from (4.9) at the following representation for the mid-plane temperature ψ_R field of an ideal undulated pattern:

$$\psi_R(x, y) = \text{Re}[e^{iqx}(A(q, p) + B(q, p)e^{ipy} - C(q, p)e^{-ipy}) + \text{h.o.t.}]. \tag{4.13}$$

with real A, B and $C = B$ and higher-order terms neglected. It is illuminating that, slightly above the instability, ψ_R as presented in (4.13) can be considered as a phase modulation of the longitudinal-roll pattern. In fact, a modulated longitudinal-roll pattern $2A \cos(qx + \phi(y))$ with $\phi(y) = (2B/A) \sin(py)$ and $(2B/A) \ll 1$ corresponds to (4.13) in a leading-order expansion with respect to B/A .

The amplitudes A and $B = C$ obtained from (4.11) and the resulting approximate solution V according to (4.9) are convenient for generating the full nonlinear Newton iteration scheme. In this way, we construct fully three-dimensional OU solutions of the OBE of the type described in (4.7) for $R > R_u$. The subsequent linear stability analysis (see (4.8)) yields the stability regions of the OU.

Figure 5 shows the representative results for $P = 1.14$ and $\theta = 30^\circ$. The OU at a given ϵ are stable within certain regions (islands) in the (q, p) -space. These islands shrink with decreasing ϵ , becoming arbitrarily small as ϵ approaches ϵ_u . In this limit,

the island is located at $q \approx q_c$ and $p \approx 0$ and its area approaches zero. The islands reach their maximal size for $0.1 \lesssim \epsilon \lesssim 0.2$, before they shrink again as the transition to crawling rolls is approached.

The limits of the islands in figure 5 are given by amplitude instabilities ($s=0$ in (4.8)) at the low- p boundary of the islands and long-wavelength modulational instabilities ($|s| \ll q_c$) at the high- p boundary. In the former case, the amplitude A is virtually unaffected, whereas the other amplitudes in (4.13) are perturbed as follows: $B \rightarrow B + \delta$, $C \rightarrow C - \delta$, with $|\delta| \ll B$. Due to the asymmetry $B \neq C$, a non-vanishing component U_x develops, i.e. a mean flow which probably drives the defect-turbulent state. By analogy to the aligning effect of the basic profile U_0 on the longitudinal rolls, U_x will tend to turn the roll axis as well.

In contrast to the amplitude instabilities, the modulational instabilities (which involve finite Floquet vectors s) will change the basic periodicity of the undulation solutions. The main consequence of such a perturbation involves a mean-flow (along \hat{x}) contribution to \mathbf{v}_{tor} , which presumably induces defect chaos as well.

4.3. Simulations

Since the Galerkin method is restricted to the analysis of stationary periodic states and their stability, direct numerical simulations of the OBE are needed to investigate the time evolution of complex patterns. For that purpose, a previously developed code (Decker, Pesch & Weber 1994; Pesch 1996) was generalized to cover inclination (Brausch 2001). This code represents all fields by an appropriate Galerkin ansatz like (4.7) and treats the (x, y) -dependence in Fourier space by a pseudospectral technique. By using a small (<10) number of modes in the \hat{z} -direction, reliable simulations of large-aspect-ratio systems can be conducted on common computer clusters in a reasonable time. In the (x, y) -plane, our simulations covered areas up to $40d \times 75d$, where we used up to 384 Fourier modes in either direction. Periodic boundary conditions have been used except in a few cases, where we introduced subcritical ϵ ramps to suppress convection at the sidewalls to approximate experimental conditions. We typically found the same bulk behaviour in both cases for simulation domains of size $40d \times 40d$ or greater.

The time integration in the simulations was started either from random initial conditions (to scan the manifold of nonlinearly selected solutions) or from previously calculated Galerkin solutions with superimposed noise to check for stability. A representative example of stationary OU is shown in figure 6; the system chose wavenumbers $q = 1.05q_c = 3.26$ and $p = 0.16q_c = 0.5$, which are inside the corresponding stability island in figure 5. The resulting amplitude ratio $B/A = 0.59$ (as specified in (4.13)) agrees with the Galerkin result to within 2%. In fact, OU were always selected for small $\epsilon < 0.03$ when starting from random initial conditions. At larger ϵ OU could still be obtained by starting from a stable periodic Galerkin OU with a small amount of superimposed noise with a signal-to-noise ratio of 10^{-4} . This is demonstrated in figure 7(a). Here we started at $\epsilon = 0.10$ and $q = 1.05q_c = 3.28$, $p = 0.31q_c = 1.02$ inside the corresponding stability region in figure 5 and recovered the ideal Galerkin solution with $B/A = 0.94$. However, the basin of attraction of the OU shrinks with increasing ϵ and the simulations starting from random initial conditions typically settle into UC, as for example shown in figure 7(b). The ensuing bistability between stationary perfectly ordered solutions and dynamic weakly defect turbulent ones at larger ϵ is the main theme of this paper.

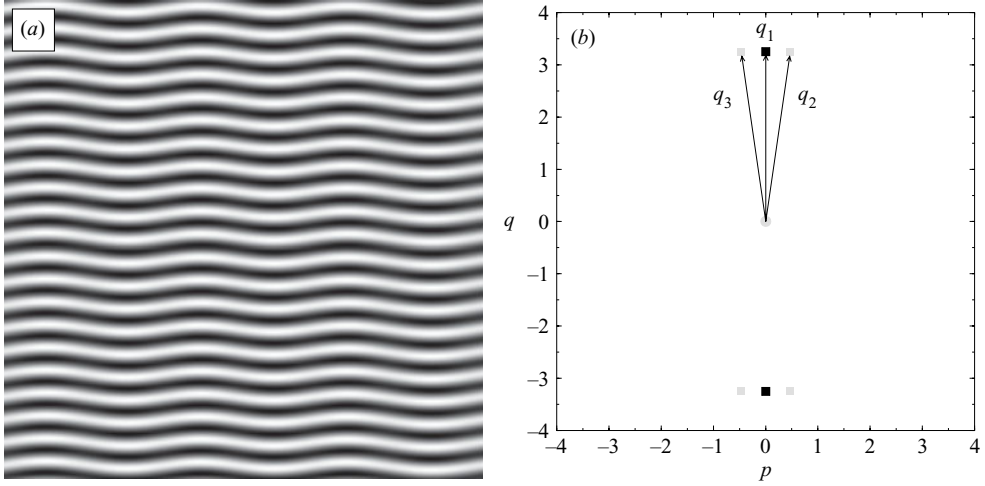


FIGURE 6. Simulation at $\gamma = 30$ and $\epsilon = 0.025$ ($R = 1750$). (a) Stationary OU after 10^5 iterations ($2000t_v$), starting from random initial conditions. (b) Fourier spectrum of (a): pattern locked perfectly into the resonant tetrad described by the amplitude equations.

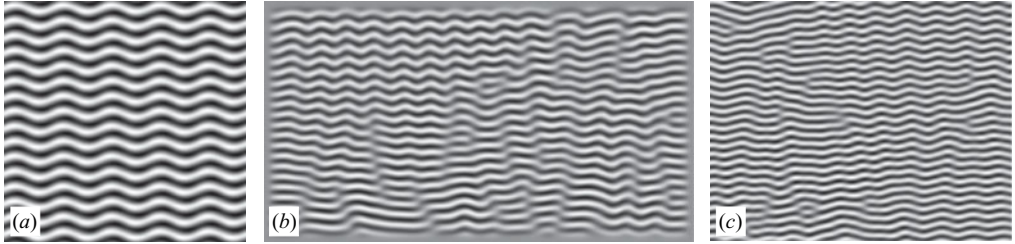


FIGURE 7. Convection patterns at $\epsilon = 0.10$ and $\gamma = 30^\circ$. (a) Numerical simulation started from the Galerkin solution with superimposed Gaussian noise, showing perfect OU after reaching steady state. (b) Numerical simulation started from Gaussian noise, with subcritical ϵ -ramp simulating lateral boundaries. OU are visible in the upper left and UC in the lower right. (c) Fourier-filtered shadowgraph image of homogeneous subregion of experimental cell.

5. Analysis of complex undulation patterns

In this section we discuss several approaches to characterizing STC in general and the onset of chaotic undulations in particular. Section 5.1 explains how we identify all topological defects in a shadowgraph image and generate a time series of the total number of defects, $N(t)$, from the consecutive images of an experimental run. Section 5.2 deals with the pattern entropy $S(t)$ and the transverse correlation length $\xi(t)$. Finally, in §5.3 we discuss the statistical properties of the amplitudes A , B , C , defined in (4.9).

5.1. Identification of defects

A shadowgraph (or simulation) image can be understood as the real part ψ_R of a complex field $\psi(x, y) = |\psi(x, y)| \exp[i\phi(x, y)]$ with modulus $|\psi|$ and phase ϕ . To construct $\psi(x, y)$, we demodulate the image as illustrated in figure 8: after a two-dimensional Fourier transformation, half of the modes in the Fourier plane are set to zero (see figure 8a). A subsequent inverse Fourier transformation recovers $\psi(x, y)$.

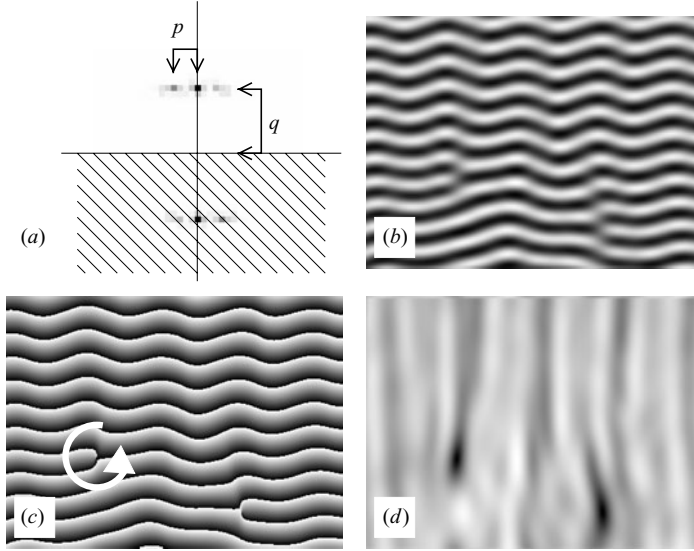


FIGURE 8. Four views of a demodulated experimental convection pattern showing undulations and defects. (a) Power spectrum ψ of experimental images, with the shaded region of Fourier space discarded during reconstruction of the complex field so that $\psi(q, p) = 0$ for $q < 0$, where (q, p) are wavenumbers associated with (\hat{x}, \hat{y}) -directions. (b) Real part ψ_R of a Fourier-filtered shadowgraph image at $\epsilon = 0.10$ with negative (left) and positive (right) defects. Uphill direction is at the left side of the page. (c) Phase field ϕ : black is $\phi = 0$ and white is $\phi = 2\pi$. The arrow indicates an integration loop around a defect as given in (5.1). (d) Modulus of image, $|\psi|$.

As already discussed above the characteristic feature of a UC pattern is undulating stripes containing topological point defects (dislocations) where an additional roll segment ends inside the bulk of the pattern. Defects locally change the spacing and orientation of the rolls and correspond to a simple root of $\psi(x, y) \equiv \psi_R + i\psi_I$, where the subscripts represent the real and imaginary parts (Bodenschatz, Pesch & Kramer 1988; Rasenat, Steinberg & Rehberg 1990; Walter, Pesch & Bodenschatz 2004). Moreover, complex analysis requires that the topological charge (or ‘winding number’) n , defined by

$$\oint \nabla\phi \cdot ds = \pm n 2\pi \quad (5.1)$$

becomes non-zero; only point defects with $|n| = 1$ are found in UC.

To locate the zeros in ψ we have used the following efficient algorithm, suggested by Egolf (private communication), which uses the fact that both ψ_R and ψ_I vanish at each defect. To begin, we formed a set of four binary fields for $\psi_R(i, j)$ at each pixel $((i, j) \in \mathbb{Z})$ of the plane:

$$\tilde{\psi}_R^{\Delta i, \Delta j}(i, j) = \begin{cases} 1, & \psi_R(i + \Delta i, j + \Delta j) > 0 \\ 0, & \text{otherwise,} \end{cases} \quad (5.2)$$

where $(\Delta i, \Delta j) \in \{(0, 0), (0, 1), (1, 0), (1, 1)\}$ denote the neighbouring pixels of (i, j) . The four binary fields $\tilde{\psi}_R^{(i, j)}$ are then logically combined at each point to produce a new binary field $\bar{\psi}_R(i, j)$:

$$\bar{\psi}_R = (\tilde{\psi}_R^{0,0} \oplus \tilde{\psi}_R^{0,1}) \vee (\tilde{\psi}_R^{0,0} \oplus \tilde{\psi}_R^{1,0}) \vee (\tilde{\psi}_R^{0,0} \oplus \tilde{\psi}_R^{1,1}), \quad (5.3)$$

where \oplus is the XOR (exclusive OR) logical operator and \vee is the OR logical operator. Analogously, we define the new binary field $\overline{\psi}_I(i, j)$. All points (i, j) , where $\overline{\psi}_R(i, j) = \overline{\psi}_I(i, j) = 1$, serve as candidates for a defect. To ensure that such a point is indeed a defect, the contour integral in (5.1) is evaluated by traversing its eight nearest neighbours. A defect candidate is accepted if the contour integral yields $\pm 2\pi$, assigning the appropriate sign to the defect based on the sign of the integral. Counting the defects (i.e. the zeros of $\psi(x, y)$) for a time series of frames yields $N(t)$.

5.2. Global stochastic properties of UC

This continues the analysis of the representative case of inclination angle $\gamma = 30^\circ$. A prominent feature of the experiments is that at higher ϵ ($\gtrsim 0.10$) the competing attractors – OU with few defects and UC with many as shown in figure 1 – are alternately visited in time, while the system remains persistently chaotic at lower ϵ . A similar bistability was also found in the case of (isotropic) Rayleigh–Bénard convection: Cakmur *et al.* (1997) observed competition between ideal rolls (IR) and the spatiotemporally chaotic state of spiral defect chaos (SDC). In that case, however, a transition from SDC to IR was observed by decreasing ϵ . There, the analysis of the spectral entropy $S(t)$ (Neufeld & Friedrich 1994) was illuminating, and the concept is applied here as well. $S(t)$ is defined as

$$S(t) = -\langle P(q, p, t) \ln P(q, p, t) \rangle, \quad (5.4)$$

where $P(q, p, t)$ is the normalized spectral distribution function that describes the power in the mode with wave vector (q, p) at time t and the average $\langle \cdot \rangle$ is performed over the (q, p) -plane.

The function $S(t)$ provides a measure for order in a pattern: we have $S = \ln 6$ for OU described by the six modes of (4.13) while a disordered pattern has more modes excited and $S > \ln 6$. In fact, within anisotropic patterns (such as undulations) the pattern entropy is even better suited for characterizing disorder than it is in isotropic systems. For instance, for convection in a horizontal layer (ordinary Rayleigh–Bénard convection), target or spiral patterns are commonly observed. The spatial power spectrum of these patterns shows a densely filled annulus of excited modes (and thus a high value for S) even though the state is well ordered. In the inclined case in which the symmetry is broken such states do not exist.

Further characterization of the relative order of the pattern is possible using the correlation length ξ in the transverse (\hat{y}) direction obtained from the half-width at half-maximum of the spatial autocorrelation functions, as demonstrated in figure 9. In figure 9(a), the pattern is disordered, the spatial autocorrelation function is sharply peaked at the origin and ξ is only a few d . In figure 9(b), the pattern is highly ordered and shows correlations that fall off with a correlation length approaching the length of the cell. Furthermore, in line with the theoretical analysis in § 5.3, inspection of figure 9 shows that the wavelength of the spatial oscillations of the autocorrelation function along the \hat{y} -direction in the disordered case is about twice the value in the ordered case.

Figure 10 shows example time traces of $N(t)$, $S(t)$ and $\xi(t)$ for $\epsilon = 0.08$ in the UC regime and also for $\epsilon = 0.17$, well above the transition to competition between UC and OU. The dashed vertical lines for the case $\epsilon = 0.17$ mark the times of the images shown in figure 1, which exemplify the cases of high S (disordered UC) and low S (ordered OU), respectively. For each time series of the quantities $X = S(t), N(t), \xi(t)$ we obtain the time average $\langle X \rangle$ and the standard deviations $\Sigma_X \equiv \sqrt{\langle X^2 \rangle - \langle X \rangle^2}$.

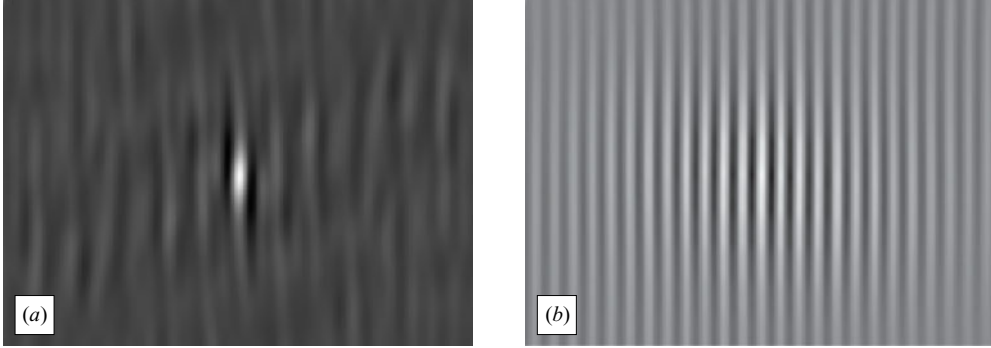


FIGURE 9. Spatial autocorrelations $\langle M(\mathbf{r})M(\mathbf{r} - \mathbf{r}_0) \rangle$ of the modulus $M = |\psi|$ of the complex demodulation functions ψ associated with the images shown in figure 1: (a) UC and (b) OU. Images are rotated by 6° clockwise with respect to the coordinate system shown in figure 1, due to a slight misalignment of the experimental cell.

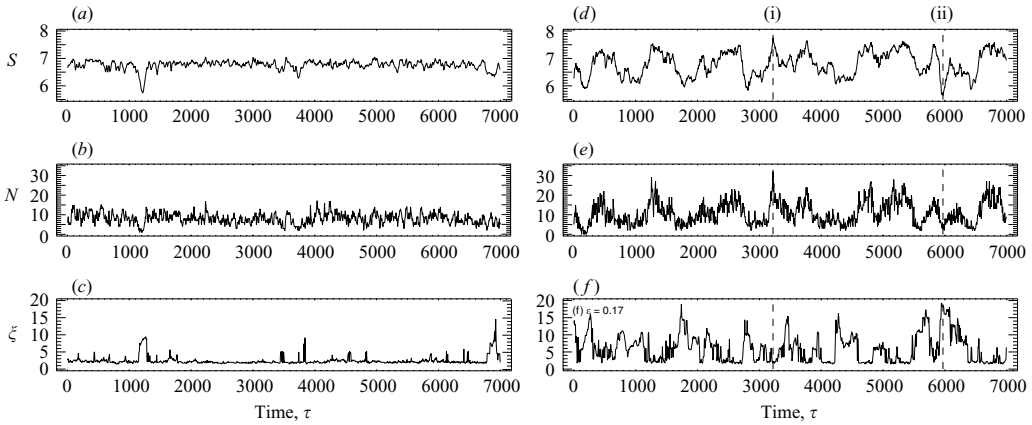


FIGURE 10. Time trace of: (a, d) spectral entropy S , (b, e) number of defects N , and (c, f) transverse correlation length ξ at $\epsilon = 0.08$ (a, b, c) and $\epsilon = 0.17$ (d, e, f), extracted from shadowgraph images. Data were sampled every 10 seconds ($6.5\tau_v$). In (d) dashed line (i) corresponds to the time of the image in figure 1(a) (UC) and line (ii) to figure 1(b) (OU).

For $\epsilon = 0.17$, the quantities $S(t)$, $N(t)$, and $\xi(t)$ show considerably larger fluctuations than at $\epsilon = 0.08$. In fact, at higher ϵ the system alternately visits the OU and UC states, and we observed a number of instances where the system remained in the OU state for more than $500\tau_v$. In ordered patterns, the values of $N(t)$ and $S(t)$ are smaller than in the disordered state, while $\xi(t)$ shows the opposite behaviour. To quantify the relation among these quantities, in figure 11 we show the temporal cross-correlations $C_{X,Y}(\Delta t) = \langle (X(t + \Delta t) - \langle X \rangle)(Y(t) - \langle Y \rangle) \rangle / (\Sigma_X \Sigma_Y)$ for $X, Y \in S(t), N(t)$, and $\xi(t)$. In all cases, the cross-correlations at $\epsilon = 0.17$ are more pronounced, in line with the larger fluctuations of $S(t)$, $N(t)$, $\xi(t)$ seen in figure 10. The cross-correlation curves are consistent with our general physical picture: the maximum in the S - N curve at $\Delta t = 0$ expresses the strong correlation between S, N at equal time while the minima in the N - ξ , ξ - S curves at $\Delta t = 0$ denote the strong anticorrelation. The secondary extrema at $|\Delta t| \approx 500\tau_v$ in figure 11 might reflect an average internal frequency (all visible to some extent in figure 10) associated with the switching between more and less ordered states. This would account for the observed anticorrelation between S

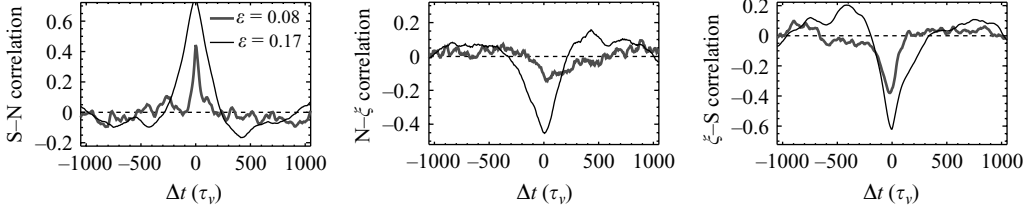


FIGURE 11. Cross-correlations $C(S, N)$, $C(N, \xi)$, $C(\xi, S)$ of spectral entropy $S(t)$, number of defects $N(t)$ and correlation length $\xi(t)$ from left to right.

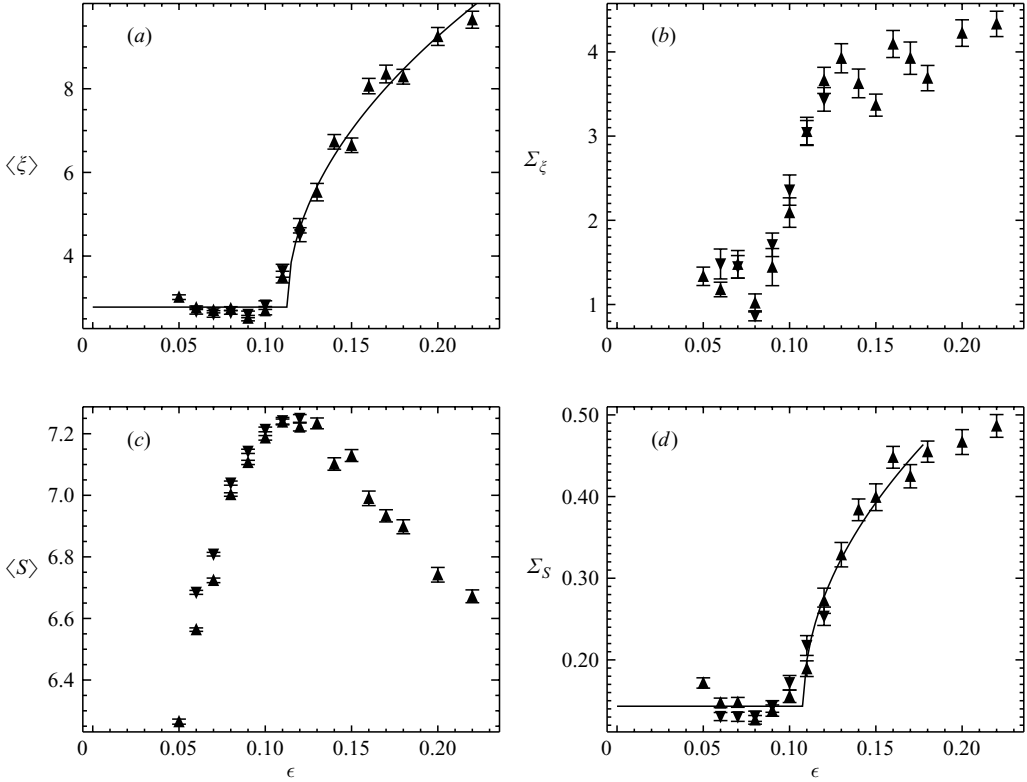


FIGURE 12. (a) Mean correlation length $\langle \xi \rangle$ and (b) its standard deviation Σ_{ξ} as a function of ϵ . (c) Mean spectral entropy $\langle S \rangle$, and (d) its standard deviation Σ_S as a function of ϵ . Solid lines $\propto \sqrt{\epsilon - \epsilon_c}$ are plotted as guides to the eye. Triangles are for short runs in which temperature steps between them were either increasing (\blacktriangle) or decreasing (\blacktriangledown).

and N with a time delay of $\Delta t \approx 500\tau_v$ and the corresponding correlations apparent in the N - ξ , ξ - S curves. Much longer experimental runs would be needed to quantify this phenomenon and the underlying mechanism; with such runs, we would expect the asymmetry of the cross-correlation functions between negative and positive Δt to vanish as well.

The transition to increasing order, i.e. the appearance of long-living OU states for $\epsilon \approx 0.1$ is a peculiar one, in that the system does not remain in the new ordered state but intermittently returns to the chaotic state. To characterize this transition we measured the quantities $\langle S \rangle$, $\langle \xi \rangle$, Σ_S and Σ_{ξ} at each ϵ ; see in figure 12. All four

plots exhibit changes near a transition point $\epsilon_t \approx 0.1$. For instance $\langle \xi \rangle(\epsilon)$ increases sharply there, indicating that the size of ordered regions is strongly growing for $\epsilon > \epsilon_t$. Both $\Sigma_S(\epsilon)$ and $\Sigma_\xi(\epsilon)$ show that the fluctuations increase in magnitude as well when $\epsilon > \epsilon_t$. No hysteresis was observed across this transition. Note that this transition also corresponds to previously described (Daniels & Bodenschatz 2002, 2003) changes in the defect dynamics above $\epsilon = 0.10$: for instance a decrease in the temporal velocity correlation.

5.3. Local amplitude analysis

The analyses presented above are not specific to UC. Thus, we have used an additional method to characterize slightly disordered undulation patterns. The idea is to use the ansatz in (4.13) locally, i.e. with real space- and time-dependent quantities (q, p, A, B, C) . The first step is to extract from our experimental images the complex function $\psi(x, y)$ as explained at the beginning of the present section (see figure 8). Then $q(x, y)$ is obtained by the local wavenumber method described in Egolf *et al.* (1998), by calculating

$$q(x, y) = \sqrt{\frac{-\partial_x^2 \psi(x, y)}{\psi(x, y)}}. \quad (5.5)$$

Near zeros of $\psi(x, y)$, for instance at topological defects, the wave-vector field $q(x, y)$ is ill-defined and yields unphysically large values, which can safely be identified and neglected. To determine the local undulation wavenumber $p(x, y)$ we use the squared modulus of ψ , which can be locally well parameterized by the following analytical expression (see (4.13)):

$$|\psi|^2(x, y) = A^2 + B^2 + C^2 - 2BC \cos(2py) + 2A(B - C) \cos(py). \quad (5.6)$$

Consequently, the local wavenumber analysis applied to each line of $|\psi|^2(x, y)$ (see figure 8d) reveals the local undulation wavenumber $p(x, y)$, which is constant for an ideally ordered undulation pattern. According to (5.6), the periodicity of $|\psi|^2$ along the \hat{y} -direction is characterized by the local wavelength $\lambda_y = \pi/p(x, y)$ in the disordered case $B \neq C$. For $B \approx C$, (5.6) reduces to

$$|\psi|^2 = A^2 + 2C^2 - 2C^2 \cos(2py) \quad (5.7)$$

and the corresponding wavelength in the ordered case is thus reduced by a factor of 2, so that $\lambda_y = \pi/(2p(x, y))$. This feature is reflected in the autocorrelation function of $|\psi(x, y)|$ (see figure 9) and has been mentioned there already.

Figure 13 shows sample wavenumber distributions of (q, p) for the experimental convection patterns cells together with the stability islands from figure 5. The mean values of q, p (the small circle) are in the stable regime. We previously observed the mean value of p to be proportional to $\sqrt{\epsilon - \epsilon_u}$, where ϵ_u agrees with the Galerkin prediction for the onset of OU (Daniels & Bodenschatz 2002). The mean roll wavenumber q does not vary significantly with ϵ . Inspection of figure 13(a) shows that the distribution of the q, p values overlaps with the stability regions in a wide range, and the most probable value (circle) is within the stable regime. Near defects, the undulation patterns are strongly deformed and local wavenumbers can be pushed outside the stability regions.

Further insight arises from distributions of the amplitudes A, B and C . For an ideal undulation pattern characterized by the constant wavenumbers q, p we also know the amplitudes A and $B = C$ according (4.11). As demonstrated in figure 13(b) the ratio C/A varies significantly with wavenumber. Thus, it is not surprising that a

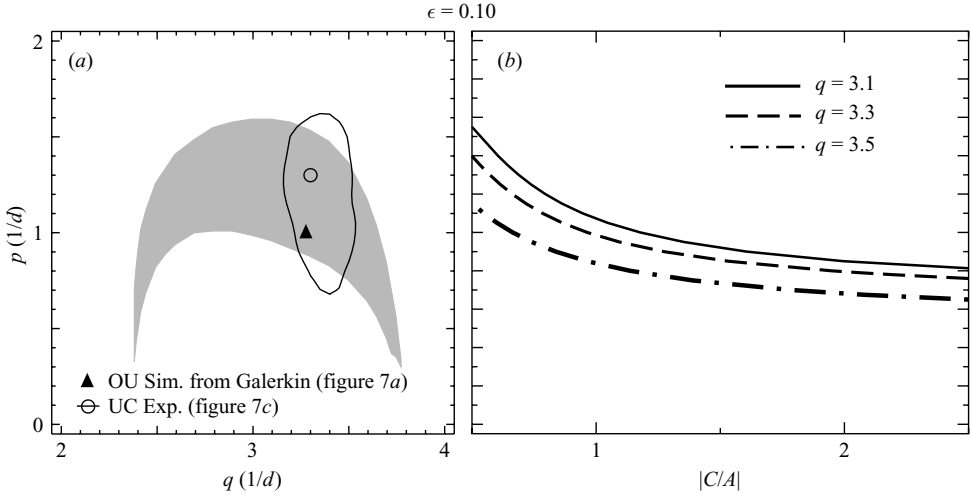


FIGURE 13. (a) Stability islands at $\epsilon=0.1$ from figure 5, showing sample wavenumber distributions for each of the images in figure 7. Peaks of the distributions are given by symbols; lines are the half-maximum of the distributions showing UC. (b) Corresponding theoretical amplitude ratios $|C/A|$ for $q = 3.1, 3.3, 3.5$ within the stable region.

disordered pattern with a fairly wide range of local q, p values (as shown in figure 13) is characterized by a broad distribution of the amplitudes $A, B \neq C$ as well.

We determined A, B and C from the local maxima and minima of the experimental $|\psi|^2$. Simple analysis of (5.6) shows that for $B \neq C$ the minima of $|\psi|^2$ within $\lambda_y = 2\pi/p$ differ in magnitude, while the maximal values are equal. This can be seen in figure 8(d), where the vertical minimal stripes differ in their greyscale values from the adjacent ones. We have recorded the differences of these neighbouring minima along each row of the $|\psi|^2$ images. A local fit to (5.6) yields the local values of B/A and C/A . Thus, we obtain an ensemble of B/A and C/A values over the whole (x, y) -plane, from which we obtain the median values shown below. The neighborhoods of defects, where the analysis fails, were left out. By comparing only the differences of neighbouring minima but not their locations, we lose any phase information of the cosine functions in (5.6), which in any case would be lost in the vicinity of defects. Also note that the transformation $y \rightarrow y + \pi/p$ results in $B \leftrightarrow C$. Thus, there is no conceptual difference between the two cases $B < C$ and $B > C$ in our dataset, and they have been combined to improve statistics. We have chosen the convention $B < C$ to present the amplitude ratios. An advantage of our amplitude analysis is its independence from $q(x, y)$ and $p(x, y)$. Furthermore, the procedure is not sensitive to a small tilts of the overall undulation pattern.

As shown in figure 14, the median value of $|C/A|$ is observed to be low (0.2) near onset and rise with ϵ . For small ϵ the peak in $|B/C|$ is near the ideal OU value $B/C = 1$. With increasing ϵ the intermittently visited UC states are responsible for an increasing asymmetry $B \neq C$, which is then reflected in the average ratio in figure 14 as well. The averages of the ratios C/A and B/C shown in figure 14 are obtained from a sequence of the corresponding distribution functions, examples of which are shown in figure 15. We observe that the distributions become slightly narrower at the higher ϵ , which might indicate the increased prevalence of OU.

One feature not important for the present analysis is a weak drift of the experimental patterns down the cell (Daniels & Bodenschatz 2002). This is also the reason why

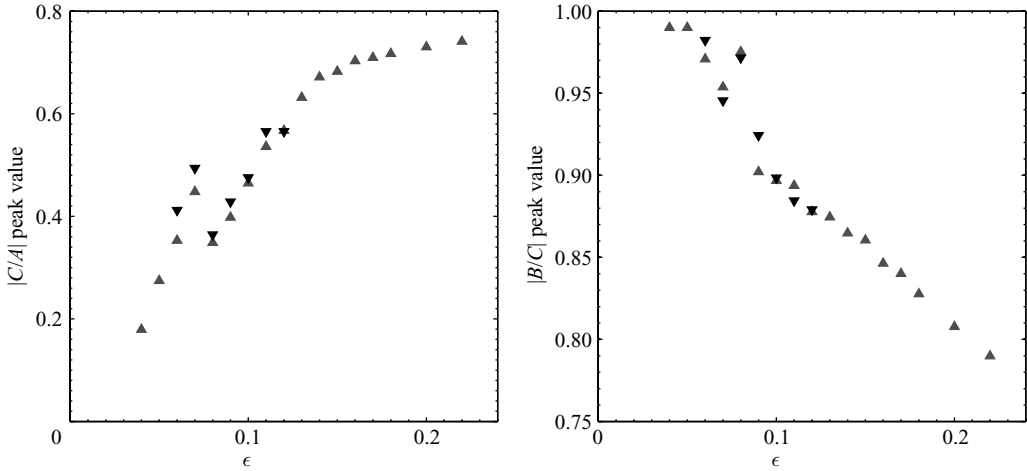


FIGURE 14. Ratios $|C/A|$ and $|B/C|$ as a function of ϵ , measured at the peak value of the histogram. Symbols represent averages from 500 experimental images, for which quasi-static temperature steps are increasing for \blacktriangle and decreasing for \blacktriangledown .

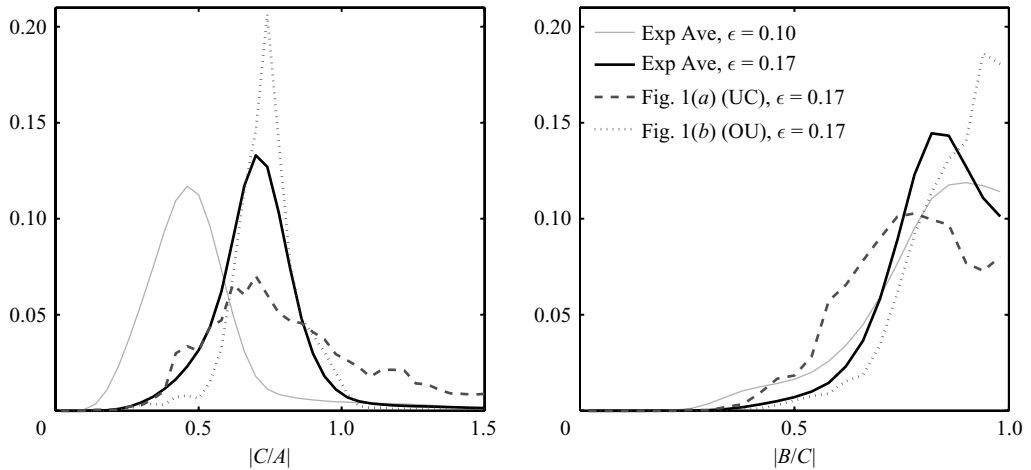


FIGURE 15. Histograms of $|C/A|$ and $|B/C|$ at two values of ϵ . Averaged experimental points (solid) are taken over 500 images, with comparison to single images (dashed, dotted) as specified in legend for $\epsilon = 0.17$.

undulations are mostly invisible in the time-averaged image shown in figure 4(b). We associate the drifting behaviour with non-Boussinesq effects, which combined with the effect of the basic shear render the growth rates of σ_B , σ_C of the oblique modes in (4.11b) and (4.11c) complex. Between $\epsilon = 0.08$ and $\epsilon = 0.17$ a drift speed of about $0.05d/\tau_v$ has been measured, which is substantially smaller than the value $d/\tau_v \approx 1$ observed above γ_{c2} . The difference may be partially accounted for by the strength of the shear flow, which is greater for steeper inclinations.

6. Discussion

The central topic of this work is the analysis of the competition between OU and UC. The Galerkin analysis of the OBE demonstrates the existence of linearly stable

undulation patterns above the wavy instability up to fairly large ϵ . As shown in figure 5 the wavenumbers q , p , which characterize the three dominant modes A , B , C (equation 4.13) cover a finite region in \mathbf{q} -space, which is maximal near $\epsilon = 0.1$. The linear stability of OU is confirmed by direct simulations of the OBE when starting from a Galerkin solution with noise (see figure 7a). However, the basin of attraction of the OU shrinks with increasing ϵ . At small ϵ starting from random initial conditions the system selects OU (see figure 7a), albeit after a long transient. In contrast, at larger ϵ the system seems to remain in a UC state that competes with regions of OU (see figure 7b). Within the spatial and temporal limitations of our simulation we are unable to determine whether we observe UC as a long-lived transient or as a truly asymptotically selected state.

In the experiment we do not observe ideal OU in any regime. At small ϵ , for instance at $\epsilon = 0.08$, the number of defects N in our sample area (the box in figure 4) varies between 3 and 18; the average is about $N = 10$ with fluctuations between these extrema (see figure 10b). For larger ϵ the situation is different (see figure 10d). We find an intermittent switching between states with very few defects (~ 4 in figure 1b) and others with many (up to $N \gtrsim 25$), as in figure 1(a). On the other hand, the system can remain for long times in either of these states, switching intermittently between them.

We interpret this scenario as reflecting the competition between OU and UC states. Defects distort the patterns and may even produce regions of the cells where part of the the wavenumber distribution lies outside the stability regions. The creation of defects and their dynamics is a well-known mechanism allowing the system to return to the stable regime. In the optimal case, this is achieved when oppositely charged defects annihilate each other or move to the boundaries. This process takes time and is susceptible to imperfections in the cell (particularly the boundaries), but there are also cases (such as SDC; Bodenschatz *et al.* 2000) where the system never settles down to the stable attractor but switches intermittently back and forth between almost perfect ordered and strongly disordered states as in our case.

In contrast to similar and previously studied anisotropic systems like the electrohydrodynamic instability in nematic liquid crystals (Rasnat *et al.* 1990), the basic equations in inclined layer convection are simple enough to be amenable to a precise theoretical analysis. Therefore, we have been able to characterize the ideally ordered undulation patterns and their stability in three dimensions, and the evolution of these states into those with higher complexity has been described by direct numerical solutions of the underlying Boussinesq equations. In addition, we have analysed experimental results from the same regime using a variety of pattern analysis methods, including defect statistics and correlation functions, providing a means of direct comparison of theory, simulation and experiment. Through these analyses, we have demonstrated the crucial importance of topological defects in the competition between chaotic and well-ordered patterns. While numerical simulations demonstrate stable ordered undulations over a range of ϵ above the secondary instability, such a state is only intermittently accessible in experiments. Interestingly, this ordered state is more prevalent at *higher* driving, where the stability region for the undulations is largest.

Motivated by the theoretical analysis, we have analysed our system using not only established methods, but also quantities specifically tailored for the particular type of disorder discussed in this paper. In this way, we have arrived at a reduced dynamical description in terms of the undulation amplitudes, which represent the complexity of the actual system in a clear manner. An interesting extension to this approach

would be to map these complex spatiotemporal dynamics to a system of generic Ginzburg–Landau equations; for a recent example see Madruga, Riecke & Pesch (2006).

We wish to thank J. P. Sethna and R. J. Wiener for helpful discussions regarding this work. We thank G. Ahlers for providing us with the code to determine the material parameters. KED and EB acknowledge support from the National Science Foundation for support under grant DMR-0072077. KED thanks the Isaac Newton Institute for Mathematical Sciences for their hospitality and support which allowed the preparation of this manuscript.

REFERENCES

- ANDERECK, C. D., LIU, S. S. & SWINNEY, H. L. 1986 Flow regimes in a circular Couette system with independently rotating cylinders. *J. Fluid Mech.* **164**, 155–183.
- BLONDEAUX, P. 1990 Sand ripples under sea waves. Part 1. Ripple formation. *J. Fluid Mech.* **218**, 1–17.
- BODENSCHATZ, E., PESCH, W. & AHLERS, G. 2000 Recent developments in Rayleigh–Bénard convection. *Annu. Rev. Fluid Mech.* **32**, 709–778.
- BODENSCHATZ, E., PESCH, W. & KRAMER, L. 1988 Structure and dynamics of dislocations in anisotropic pattern-forming systems. *Physica D* **32** (1), 135–145.
- BOTTIN, S., DAVIAUD, F., MANNEVILLE, P. & DAUCHOT, O. 1998 Discontinuous transition to spatiotemporal intermittency in plane Couette flow. *Europhys. Lett.* **43**, 171–176.
- BRAUSCH, O. 2001 Rayleigh–Bénard Konvektion in verschiedenen isotropen und anisotropen Systemen. PhD thesis, Universität Bayreuth.
- DE BRUYN, J. R., BODENSCHATZ, E., MORRIS, S. W., TRAINOFF, S. P., HU, Y., CANNELL, D. S. & AHLERS, G. 1996 Apparatus for the study of Rayleigh–Bénard convection in gases under pressure. *Rev. Sci. Instrum.* **67**, 2043–2067.
- CAKMUR, R. V., EGOLF, D. A., PLAPP, B. B. & BODENSCHATZ, E. 1997 Bistability and competition of spatiotemporal chaotic and fixed point attractors in Rayleigh–Bénard convection. *Phys. Rev. Lett.* **79**, 1853–1856.
- CHANDRASEKHAR, S. 1961 *Hydrodynamic and Hydromagnetic Stability*. Oxford University Press.
- CLEVER, R. M. 1973 Finite amplitude longitudinal convection rolls in an inclined layer. *Trans. ASME C*: **95**, 407–408.
- CLEVER, R. M. & BUSSE, F. H. 1977 Instabilities of longitudinal convection rolls in an inclined layer. *J. Fluid Mech.* **81**, 107–125.
- COULLET, P., ELPHICK, C., GIL, L. & LEGA, J. 1987 Topological defects of wave patterns. *Phys. Rev. Lett.* **59** (8), 884–887.
- CROSS, M. C. & HOHENBERG, P. C. 1993 Pattern formation out of equilibrium. *Rev. Mod. Phys.* **65**, 851–1112.
- CROSS, M. C. & HOHENBERG, P. C. 1994 Spatiotemporal chaos. *Science* **263**, 1569–1570.
- DANIELS, K. E. & BODENSCHATZ, E. 2002 Defect turbulence in inclined layer convection. *Phys. Rev. Lett.* **88**, 034501.
- DANIELS, K. E. & BODENSCHATZ, E. 2003 Statistics of defect motion in spatiotemporal chaos in inclined layer convection. *Chaos* **13**, 55.
- DANIELS, K. E., PLAPP, B. B. & BODENSCHATZ, E. 2000 Pattern formation in inclined layer convection. *Phys. Rev. Lett.* **84**, 5320–5323.
- DECKER, W., PESCH, W. & WEBER, A. 1994 Spiral defect chaos in Rayleigh–Bénard convection. *Phys. Rev. Lett.* **73**, 648–651.
- ECHEBARRIA, B. & RIECKE, H. 2000 Stability of oscillating hexagons in rotating convection. *Physica D* **143**, 187–204.
- EGOLF, D. A., MELNIKOV, I. V. & BODENSCHATZ, E. 1998 Importance of local pattern properties in spiral defect chaos. *Phys. Rev. Lett.* **80**, 3228–3231.
- EGOLF, D. A., MELNIKOV, I. V., PESCH, W. & ECKE, R. E. 2000 Mechanisms of extensive spatiotemporal chaos in Rayleigh–Bénard convection. *Nature* **404**, 733–736.

- GLUCKMAN, B. J., MARCO, P., BRIDGER, J. & GOLLUB, J. P. 1993 Time averaging of chaotic spatiotemporal wave patterns. *Phys. Rev. Lett.* **71**, 2034–2037.
- GOLLUB, J. P. 1994 Spirals and chaos. *Nature* **367**, 318.
- GOLLUB, J. P. & CROSS, M. C. 2000 Nonlinear dynamics – chaos in space and time. *Nature* **404**, 710–711.
- HANSEN, J. L., HECKE, M. VAN, ELLEGAARD, C., ANDERSEN, K. H., BOHR, T., HAANING, A. & SAMS, T. 2001 Stability balloon for two-dimensional vortex ripple patterns. *Phys. Rev. Lett.* **87**, 204301.
- HART, J. E. 1971*a* Stability of the flow in a differentially heated inclined box. *J. Fluid Mech.* **47**, 547–576.
- HART, J. E. 1971*b* Transition to a wavy vortex regime in convective flow between inclined plates. *J. Fluid Mech.* **48**, 265–271.
- KELLY, R. E. 1977 The onset and development of Rayleigh-Bénard convection in shear flows: A review. In *Physicochemical Hydrodynamics* (ed. D. B. Spalding), pp. 65–79. Advanced Publications.
- KELLY, R. E. 1994 The onset and development of thermal convection in fully developed shear flows. *Adv. Appl. Mech.* **31**, 35.
- KRAMER, L. & PESCH, W. 1995 Convection instabilities in nematic liquid-crystals. *Annu. Rev. Fluid Mech.* **27**, 515–541.
- KURT, E., BUSSE, F. H. & PESCH, W. 2004 Hydromagnetic convection in a rotating annulus with an azimuthal magnetic field. *Theore. Comput. Fluid Dyn.* **18** (2–4), 251–263.
- MADRUGA, S., RIECKE, H. & PESCH, W. 2006 Defect chaos and bursts: Hexagonal rotating convection and the complex ginzburg-landau equation. *Phys. Rev. Lett.* **96** (7), 074501.
- MORRIS, S. W., BODENSCHATZ, E., CANNELL, D. S. & AHLERS, G. 1993 Spiral defect chaos in large aspect ratio Rayleigh-Bénard convection. *Phys. Rev. Lett.* **71**, 2026–2029.
- MÜLLER, H. W., LÜCKE, M. & KAMPS, M. 1992 Transveral convection patterns in horizontal shear-flow. *Phys. Rev. A* **45**, 3714–3726.
- NEUFELD, M. & FRIEDRICH, R. 1994 Pattern formation in rotating Bénard convection. *International J. Bifurcation Chaos Appli. Sci. and Engng* **4**, 1155–1163.
- NING, L., HU, Y., ECKE, R. E. & AHLERS, G. 1993 Spatial and temporal averages in chaotic patterns. *Phys. Rev. Lett.* **71**, 2216–2219.
- PAUL, M. R., CHIAM, K. H., CROSS, M. C. & FISCHER, P. F. 2004 Rayleigh-Bénard convection in large-aspect-ratio domains. *Phys. Rev. Lett.* **93**, 064503.
- PESCH, W. 1996 Complex spatiotemporal convection patterns. *Chaos* **6**, 348–357.
- RAMAZZA, P. L., RESIDORI, S., GIACOMELLI, G. & ARECCHI, F. T. 1992 Statistics of topological defects in linear and nonlinear optics. *Europhys. Lett.* **19**, 475–80.
- RASENAT, S., STEINBERG, V. & REHBERG, I. 1990 Experimental studies of defect dynamics and interaction in electrohydrodynamic convection. *Phys. Rev. A* **42** (10), 5998–6008.
- REHBERG, I., RASENAT, S. & STEINBERG, V. 1989 Traveling waves and defect-initiated turbulence in electroconecting nematics. *Phys. Rev. Lett.* **62**, 756–9.
- RUTH, D. W. 1980 On the transition to transverse rolls in inclined infinite fluid layers-steady solutions. *Intl J. Heat Mass Transfer* **23**, 733–737.
- RUTH, D. W., RAITBY, G. D. & HOLLANDS, K. G. T. 1980 On the secondary instability in inclined air layers. *J. Fluid Mech.* **96**, 481–492.
- TAGG, R. 1994 The Couette-Taylor problem. *Nonlinear Scie. Today* **4**, 1–24.
- TRAINOFF, S. P. & CANNELL, D. S. 2002 Physical optics treatment of the shadowgraph. *Phys. Fluids* **14**, 1340–1363.
- WALTER, TH., PESCH, W. & BODENSCHATZ, E. 2004 Dislocation dynamics in Rayleigh-Benard convection. *Chaos* **14** (3), 933–939.
- YOUNG, Y. N. & RIECKE, H. 2003 Penta-hepta defect chaos in a model for rotating hexagonal convection. *Phys. Rev. Lett.* **90**, 134502.
- YU, C. H., CHANG, M. Y. & LIN, T. F. 1997 Structures of moving transverse and mixed rolls in mixed convection of air in a horizontal plane channel. *Intl J. Heat Mass Transfer* **40** (2), 333–46.